

Probing the energy-dependent temporal nature of MAXI J1803-298 with *AstroSat* and *NICER*

ARBIND PRADHAN,¹ AKASH GARG,² RANJEEV MISRA,² AND BIPLOB SARKAR^{1,*}

¹*Department of Applied Sciences, Tezpur University, Napaam, Assam 784028, India*

²*Inter-University Centre for Astronomy and Astrophysics (IUCAA), Pune, Maharashtra 411007, India*

ABSTRACT

We performed the spectral and temporal analysis of MAXI J1803-298 using *AstroSat*/LAXPC and *NICER* observations taken in May 2021 during the initial phase of the outburst. We found that the source traverses through the hard, intermediate, and soft spectral states during the outburst. The spectrum in all states can be described using soft emissions from the thermal disk and hard emissions from the coronal regions. The variation in the inner disk temperature and normalization of the disk indicates the motion of the truncated disk across these different spectral states. We confirmed the presence of broad features, Type-C, and Type-B QPOs in the power spectra of different spectral states. We investigated the fractional rms and lags of all the variability features and discovered that the lag swung between positive and negative during the outburst evolution. While modeling the features with a simple model that considers variations in accretion parameters such as the accretion rate, heating rate, and inner disk radius, along with delays between them, we found a dynamic reversal in the origin of variability between the corona and the disk. Furthermore, our results are consistent with previous works and a radio study conducted on this source during its outburst.

Keywords: accretion disks – black hole physics – X-rays binaries: individual (MAXI J1803-298) — X-rays: stars

1. INTRODUCTION

X-ray binaries (XBs) are binary systems comprising a compact object and a companion star that prominently emit in the X-ray part of the electromagnetic spectrum. The compact object can either be an accreting black hole (BH) or a neutron star (NS). Depending on the mass of the companion star, XBs are classified as low-mass X-ray binaries (LMXBs) or high-mass X-ray binaries (HMXBs) (Lewin et al. 1997). HMXBs are mostly persistent, while LMXBs are transient and often remain in a low flux, quiescence state. Once an LMXB undergoes an outburst, the flux will increase, remaining high for weeks to months before slowly declining. This increase in luminosity is due to the increase in the accretion rate onto the compact object.

Most known BH XBs (or BHXBs) are transient in nature. During the outburst, a BHXB evolves through different spectral states before going back to its quiescent state and traces a ‘Q’ shaped trajectory in the hardness intensity diagram (HID; Homan & Belloni 2005; Belloni et al. 2005a; Nandi et al. 2012). The trajectory follows

a sequence: Low-Hard State (LHS)-Hard Intermediate State (HIMS)-Soft Intermediate State (SIMS)-High-Soft State (HSS), then reverses through SIMS-HIMS-LHS (Belloni & Motta 2016). This transition exhibits hysteresis where high flux causes a transition from LHS to HSS, and then as the flux gets low, the source transits back into the LHS (Miyamoto et al. 1995; Kylafis & Belloni 2015).

Typically, the outburst starts with a faint brightness, and the X-ray emission is dominated by a hard power law of $\Gamma \sim 1.5$ in LHS, accompanied by steady radio jets due to synchrotron emission. As the X-ray emission starts getting dominated by the thermal emission from the disk, the source proceeds towards HIMS and SIMS. Once the X-ray emission is prominently dominated by the soft photons, the HSS will be achieved. In the midst of this transition from LHS to HSS, radio emission quenches but recovers back during the transition to LHS (Dunn et al. 2010). For the transition from LHS to HSS, there are discrete ejections for collimated jets. According to the truncated disk model, the accretion disk is initially truncated in LHS, with soft photons from the disk being inversely Comptonized in the hot region near the BH, leading to a non-thermal power-

* E-mail: biplobs@tezu.ernet.in

law dominated photon spectrum (Sunyaev & Titarchuk 1980; Titarchuk 1994). Further, as the source moves to the soft state, the truncated disk is believed to move towards the innermost stable circular orbit (ISCO) and emits the thermal spectrum prominently. Such a thermal emission is often described using the multicolor disk blackbody model (Mitsuda et al. 1984). However, in the intermediate states, the spectrum consists of both thermal and non-thermal components. Additionally, there is another component that arises from the interaction between the hard X-rays and the disk, known as the reflection component, which can be seen as the fluorescent and reprocessed emission such as the broad, asymmetric Fe $K\alpha$ line between 6 and 7 keV (Laor 1991) and the Compton hump above ~ 15 keV (Miller 2007).

XBs exhibit variability in their light curves in the form of broadband noise (BBN) and aperiodic oscillations known as quasi-periodic oscillations (QPO) (van der Klis 2005). Using Fourier techniques, BBN and QPO can be detected as a broad and narrow peak in the power density spectrum (PDS). It is crucial to understand the QPOs, as they are believed to be produced from the proximity of a compact object and can thereby reveal the behavior of the matter in the vicinity of a strong gravitational field. QPOs are broadly classified as low-frequency QPOs (a few mHz to ~ 30 Hz) and high-frequency QPOs (also known as kHz QPOs in neutron star XBs (NSXBs); Motta 2016). High frequency QPOs have also been reported in BHXBs such as GRS 1915+105 (Belloni & Altamirano 2013) and IGR J17091-3624 (Altamirano & Belloni 2012). On the basis of intrinsic properties like centroid frequency, width, and strength, low-frequency QPOs are further classified as types A, B, and C. Interestingly, different spectral states exhibit different types of low-frequency QPO (Wijnands et al. 1999; Homan et al. 2001; Casella et al. 2004), indicating a correlation between the spectral and temporal behavior of XBs.

Although several models have been proposed to understand the physics of QPOs (mainly type-C QPOs), there is still no consensus on the exact origin of the QPOs. These models are either based on the geometrical effect or thermal instabilities in the accretion disk. For instance, models like the Relativistic Precession Model (RPM) (Stella et al. 1999; Ingram et al. 2009) are based on the geometric origin, while models like the transition layer model (Titarchuk & Osherovich 1999; Titarchuk & Fiorito 2004) are based on instability leading to the production of low frequency QPOs. Along with these models there are models based on the shock oscillation causing the low frequency QPOs in BHXBs such as Molteni et al. (1999); Chakrabarti & Manickam (2000). There

is an alternate approach based on the observed correlations between spectral and temporal properties of XBs. It has been confirmed in many sources that the QPO centroid frequency has strong correlations with spectral parameters (e.g. Garg et al. (2022); Dhaka et al. (2023) and references therein), indicating a connection between the radiative properties of accretion and QPOs. The QPOs possess energy-dependent properties such as fractional root mean square (rms) and time lag, which can be directly connected with spectral variations. These properties can help identify the radiative mechanisms responsible for the presence of QPOs. Lee et al. (2001), Kumar & Misra (2014), and Karpouzas et al. (2020) proposed models based on the idea of the Comptonized photons impinging back onto the seed photon source to describe the occurrence of hard and soft time lags for kHz QPO in NSXBs. Furthermore, based on the same framework, Karpouzas et al. (2021), Bellavita et al. (2022), and García et al. (2022) explained the observed energy-dependent rms and lag for low-frequency QPOs in BHXB. Misra & Mandal (2013), Mir et al. (2016) and Maqbool et al. (2019) considered variations in spectral parameters like accretion rate, inner disk radii, and power law index, along with propagation delays between them, to model the rms and time delays for the QPOs in NS and BH systems.

Garg et al. (2020) formulated a generic technique to model the timing behavior of variability using the spectral information of the accretion flow. The technique requires modeling the time-averaged photon spectra to determine spectral components such as the disk blackbody and thermal Comptonization of the X-ray emission. Further, in the approach, the spectral parameters are translated into their physical counterparts to determine which variations in physical parameters can reproduce the observed rms and lag associated with QPO or BBN. Garg et al. (2020) applied their model to study the temporal nature of GRS 1915+105. Similarly, Garg et al. (2022) studied the QPOs observed in MAXI J1535-371 using the model and found that the variations in the mass accretion rate, inner disk radius, and heating rate, along with delays between them could properly fit the rms and time lag spectra. Husain et al. (2023) also used this technique to investigate the QPOs and harmonics observed in H 1743-322. Recently, Tanenia et al. (2024) and Dhaka et al. (2024) also applied the technique to the energy-dependent rms and time lags of broad features, often observed in the PDS of BH systems, GX 339-4 and GRS 1915+105, respectively. This technique has been successfully applied to NSXBs, in sources such as 4U 1608-52 (Bhattacharjee et al. 2024a) and GX 9+9 (Bhattacharjee et al. 2024b).

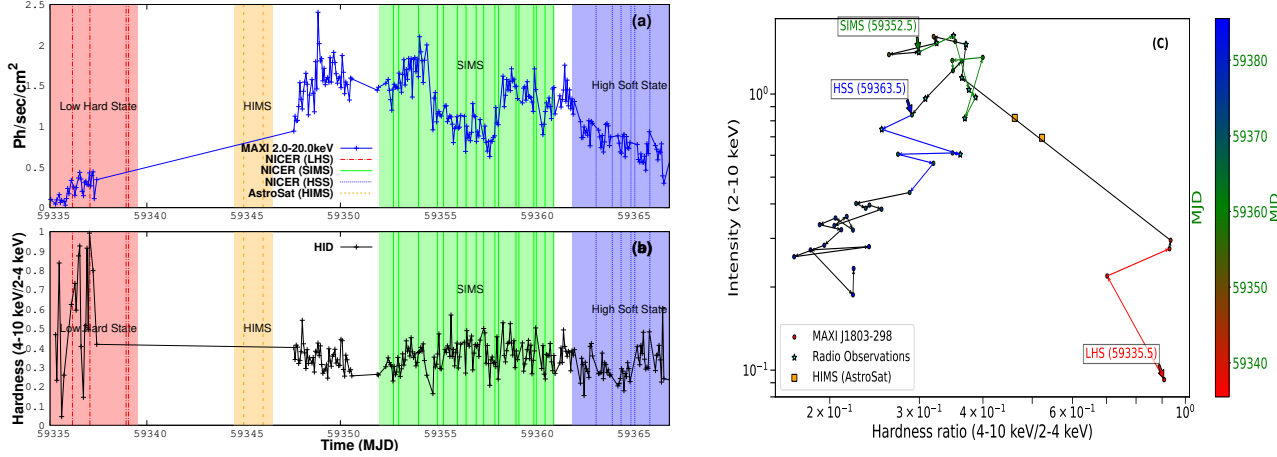


Figure 1. The figure (a) shows the MAXI light curve of MAXIJ1803 in 2-20 keV. The vertical lines represent observations taken by *NICER* (red, green, and blue) and *AstroSat* (orange). The different colors represent different spectral states: LHS (red), HIMS (orange), SIMS (green), and HSS (blue). The figure (b) shows hardness variations vs. time with hardness defined as 4-10 keV/2-4 keV. While figure (c) is the Hardness-Intensity Diagram (HID) of MAXIJ1803. The horizontal axis represents the hardness ratio (4-10 keV/2-4 keV), and the vertical axis is the intensity in 2-10 keV. The different colors represent different spectral states, and the stars on the plot represent the radio emission as taken from Wood et al. (2023). The different MJD box markers show the start of the indicated spectral state.

The BH candidate MAXI J1803-298 (hereafter, MAXIJ1803) is one of the recently discovered X-ray transients during its outburst on May 1, 2021, by *Monitor of All-sky X-ray Image/Gas Slit Camera* (MAXI/GSC) (Serino et al. 2021). The optical counterpart of the source was detected by *Swift* (Gropp et al. 2021; Hosokawa et al. 2021). Optical *Southern African Large Telescope* (SALT) spectroscopy suggested the presence of the accreting BH in MAXIJ1803 (Buckley et al. 2021). The multi-wavelength follow-up of MAXIJ1803 was performed by Mata Sánchez et al. (2022), which also suggested the compact object to be a BH with a mass of 3-10 M_{\odot} . During its initial outburst, the detection of periodic absorption dips indicated the source with high inclination ($\gtrsim 70^{\circ}$) and the periodicity was of ~ 7 hours (Homan et al. 2021; Xu & Harrison 2021; Jana et al. 2022). Radio wavelength was detected in the initial outburst phase with *MeerKAT* (Espinasse et al. 2021). Chand et al. (2022) stated that the source was in HIMS with detection of type-C QPO and estimated BH mass of $\sim 8-16 M_{\odot}$ with a spin ‘ a ’ of $\gtrsim 0.7$ using the *Astrosat* observation. Later on, Jana et al. (2022) also supported the transitioning from HIMS to SIMS using the *Astrosat* observations. MAXI/GSC monitored the source during its whole outburst, but it was unable to observe MAXIJ1803 for eight days from May 4 (MJD 59338) to May 12 (MJD 59346). Shidatsu et al. (2022) studied the X-ray spectral evolution with MAXI/GSC and *Swift*/BAT data and showed the transition from LHS to HSS. MAXIJ1803 remained in the

outburst phase till October 19 (MJD 50906) (Steiner et al. 2021). Based on *Nuclear Spectroscopic Telescope Array* (*NuSTAR*) and the *Neutron Star Interior Composition Explorer* (*NICER*) data, Feng et al. (2022) estimated the spin to be ~ 0.991 with an inclination ‘ i ’ of $\sim 70^{\circ}$. Coughenour et al. (2023) also constrained the inclination of the accretion disk to $\sim 75^{\circ}$ using *NuSTAR* data and reported type-B and type-C QPOs. Zhu et al. (2023) reported type-C QPOs using *Insight*-HXMT data and type-B QPOs using *NICER* data in different spectral states. Recently, Adegoke et al. (2024) studied the source in its LHS, intermediate, and HSS using *NuSTAR* and *NICER* and reported the presence of disk wind and dips in light curve due to the presence of photo-electric absorption.

Here, we intend to perform spectral and temporal analysis of the source in all its transitioned spectral states using the *NICER* and *AstroSat*/LAXPC observations taken during the month of May 2021. *NICER* observations are in LHS (represented by HS segment), SIMS (represented by SIMS1, SIMS2, SIMS3, and SIMS4 segments), and HSS (represented by HSS segment), and to fill the gap of HIMS, we are using *AstroSat* observations (denoted by HIMS segment). We are considering these two missions because of their excellent timing resolutions. The results of spectral analysis are used to model the energy-dependent properties with Garg et al. (2020, 2022) to understand the QPOs and the aperiodic humps observed in the PDS. Furthermore, we will try to understand the cause and the propaga-

tion of the variability based on the results of modeling by Garg et al. (2020, 2022). Figure 1 illustrates the profile of MAXIJ1803 during its outburst using MAXI observations. The source can be seen to transit through different spectral states, which we represent using different colors. In the following sections, we describe how we identify these different spectral states using spectral analysis, types of QPO observed in these states, and information from the previous works (see Mata Sánchez et al. 2022; Shidatsu et al. 2022; Wood et al. 2023). Throughout this paper, we follow the color codes used in Figure 1 to denote different spectral states.

The structure of this paper is as follows: In Section 2, we discuss the observation and data reduction. Section 3 presents the detailed spectro-timing analysis and the modeling of the energy-dependent rms and time lag spectra. We have interpreted the results obtained from our analysis in Section 4.

2. OBSERVATION AND DATA REDUCTION

2.1. *AstroSat* Observation

AstroSat is India's first multi-wavelength astronomical satellite, which performs broadband coverage from optical to hard X-rays (Agrawal 2006; Singh 2022). It consists of five payloads, namely Ultra-violet Imaging Telescopes (UVIT), Large Area X-ray Proportional Counters (LAXPC), Soft X-ray Telescope (SXT), Cadmium-Zinc-Telluride Imager (CZTI), and Scanning Sky Monitor (SSM). Among its five payloads, we have used data from Large-area X-ray Proportional Counters (LAXPC, Antia et al. 2017; Yadav et al. 2016a) and Soft X-ray Telescope (SXT, Singh et al. 2017, 2021; Bhattacharyya et al. 2021).

Both LAXPC and SXT took two Target of Opportunity (ToO) observations of MAXIJ1803 from May 11 at 01:09 UTC to May 11 at 11:59 UTC (hereafter, we call this A1) and from May 11 at 12:05 UTC to May 12 at 13:03 UTC (hereafter, we call this A2). Table 1 gives the observation IDs and exposure time details.

2.1.1. LAXPC Data Reduction

Among the three LAXPC units, we used only LAXPC20 data in our analysis, as LAXPC10 has a low gain issue, while LAXPC30 is not functioning currently. We used the standard analysis software **LAXPCsoftware**¹ (LAXPCSOFT; version 2022 August 15) to process level 1 data into level 2 data. We merged both the observations (A1 and A2) using "ftmerge" and generated a single clean Eventfile. Further, we generated light curves

and spectra using the standard sub-routines available in **LAXPCsoftware**².

2.2. *NICER* Observation

The *NICER* mission was launched in 2017; since then, it has been mounted on the International Space Station (ISS). It has good spectral and timing capabilities with a large collecting area at ~ 1 keV and a timing resolution of 300 nanoseconds (Gendreau & Arzoumanian 2017). X-ray timing instrument (XTI; (Gendreau et al. 2016)) onboard *NICER* consists of 56 co-aligned X-ray concentrator optics and silicon drift detector pairs. It provides an effective area of 1900 cm² at ~ 1.5 keV and an energy resolution of ~ 100 eV. The sensitive energy range of *NICER* is 0.2 - 12 keV (Arzoumanian et al. 2014).

NICER observed MAXIJ1803 almost through the full outburst from May 2 till November 7, 2021. In this work, we have taken 27 *NICER* observations made during May 2021, with no observations between May 6 and May 17. We analyzed these *NICER* datasets using *NICER* data analysis software (NICERDAS) (version 2023-08-22_V011a) and CALDB (version 20240206³). We reduced the *NICER* data using standard **nicerl2** pipeline⁴. Using **nicerl3-spect**⁵ task we extracted the spectra, rmf and arf. **nibackgen3C50** was chosen for the spectral background. The spectra generated by the **nicerl3-spect** task, by default, include a systematic uncertainty, which was retained during the spectral analysis. Additionally, we used **NICER_RM.Software**⁶ for extracting light curves, power spectra, rms, and time lag spectra.

Figure 1 shows the MAXI long-term light curve for May 2021 generated using the orbit data extracted from **maxi.rixen** website⁷. The dashed and solid vertical lines represent the *AstroSat* and *NICER* observations of the source, respectively. The lower panel of Figure 1 shows the evolution of the hardness of the source with time. The color codes represent different spectral states of the source during the outburst. *AstroSat* observed the source during HIMS (Chand et al. 2022; Jana et al. 2022), whereas *NICER* covered LHS, SIMS, and HSS portions (Zhu et al. 2023; Zhang et al. 2024)

² <http://astrosat-ssc.iucaa.in/laxpcData>

³ <https://heasarc.gsfc.nasa.gov/docs/heasarc/caldb/nicer/>

⁴ <https://heasarc.gsfc.nasa.gov/lheasoft/ftools/headas/nicerl2.html>

⁵ <https://heasarc.gsfc.nasa.gov/docs/software/lheasoft/help/nicerl3-spect.html>

⁶ The **NICER_RM.Software** is a package developed by Prof. R. Misra (IUCAA) and consists of subroutines similar to LAXPC software, to analyze *NICER* data.

⁷ http://maxi.riken.jp/star_data/J1803-298/J1803-298.html

¹ <http://astrosat-ssc.iucaa.in/laxpcData>

of the outburst. Figure 1 (c) shows the HID generated using MAXI one-day binned data with different spectral states marked using the same color codes as in Figure 1. There were no data from 59341.5 to 59347.5 as MAXI was off during that period, so we have marked the *AstroSat* (HIMS) observations in Figure 1 (c) using the MJD of *AstroSat* observations. The star markers in Figure 1 (c) represent radio monitoring of MAXIJ1803 through intermediate and soft states, as carried out by Wood et al. (2023) using the Very Long Baseline Array (VLBA) observations between 2021 May 13 (59347.41) and 2021 June 7 (59372.34) (See Table 1 in Wood et al. 2023). Along with VLBA, Wood et al. (2023) have utilized observations of the Atacama Large Millimeter/Sub-Millimeter Array (ALMA) taken on 2021 May 11 (59345.19) and 2021 May 15 (59349.24), and the observations of the Australia Telescope Compact Array (ATCA) taken between 2021 May 11 (59345) and 2021 July 3 (59398)). On analyzing ATCA observations, they found that the spectral index ($\alpha : (S_\nu \propto \nu^\alpha)$) of the radio spectrum at the beginning of the radio flare (59345.60 ± 0.17) was -0.1 ± 0.1 . Then, in the next observation (59347.88 ± 0.03), they noticed the peak radio flux density and the steepest radio spectrum with $\alpha = -0.8 \pm 0.2$. The steepest spectral index marks the presence of an extended, optical thin transient radio jet in LMXB. Further, they observed a gradual flattening of the radio spectrum and suggested the gradual transition of states from intermediate to HSS (see Figure 2 of Wood et al. 2023). Here in Figure 1 (c), we are just denoting different states based on our analysis and previous works. The color bar represents the evolution of the different states with MJD.

We further divided the HS, HIMS, HSS, and the four SIMS segments into sub-parts to test whether the spectral and timing properties varied during these segments. However, we didn't find any significant variation in the spectral and temporal parameters and hence retained the present form of segmentation of the observations.

3. DATA ANALYSIS

3.1. Temporal Analysis

3.1.1. The Power Density Spectrum (PDS)

We started our analysis with the HIMS observation. We computed PDS for HIMS in a broad frequency range of 0.005-20 Hz and an energy band of 3-80 keV using `laxpc.find_freqflag` of LAXPC software. The PDS obtained are deadtime Poisson noise and background corrected (Yadav et al. 2016b). Further, we fitted the PDS with a model consisting of multiple Lorentzians. As reported by Chand et al. (2022) and Jana et al. (2022),

we detected Type-C QPOs in HIMS as shown in Figure 2.

Similarly, for *NICER* observations, we analyzed different observations (HS, SIMS1, SIMS2, SIMS3, SIMS4 and HSS). We computed PDS in 0.005-20 Hz in an energy band of 0.2-12 keV for all *NICER* segments using `nicer.find_freqflag` of *NICER_RM_Software*. We detected the presence of Type-B QPOs in SIMS1, SIMS2, and SIMS3 as shown in Figure 2, similar to that reported by Zhu et al. (2023) (taken during SIMS), and some aperiodic humps were observed in HS and SIMS4.

Figure 2 illustrates the PDS of all segments fitted with multiple Lorentzians. Table A1 provides the details of all the Lorentzian components used to model the PDS of all segments.

3.2. Spectral Analysis

We separately analyzed the *AstroSat* and *NICER* observations as they are not simultaneous and correspond to the different spectral states of the source. The time-averaged photon spectrum of XBs is often described using two spectral components: multicolor blackbody disk emission and thermal Comptonized emission from a hot corona. We used XSPEC components `diskbb` (Mitsuda et al. 1984) and `ThComp` (Zdziarski et al. 2020) to model the disk and coronal emissions of both the *AstroSat* and *NICER* spectra. `diskbb` has two spectral parameters: inner disk temperature (kT_{in}) and normalization (N_{Disk}) whereas `ThComp` is a convolution model with four parameters, namely spectral photon index (or optical depth) (Γ_{tau}), electron temperature (kT_e), covering fraction (cov_frac), and redshift (z).

We started by fitting the LAXPC spectra of HIMS segment. We restricted the fitting to 3-30 keV by ignoring energies beyond 30 keV because of LAXPC background uncertainties. We accounted for absorption column density (N_H) using the XSPEC model `Tbabs` (Wijnands et al. 1999). We first modeled the joint spectrum for HIMS with `Tbabs×ThComp×diskbb` and obtained a reduced χ^2 of $121.85/24 \sim 5$. The systematic error of 2% is incorporated in the analysis (Misra et al. 2017). It is to be noted that as `ThComp` model is a convolution model, we extended the energy range by applying “energies 0.01 500 1000 log”.

We further incorporated a `Gaussian` component with line energy fixed at 6.5 keV and found that the reduced χ^2 improved to $\sim 19.52/22 \sim 0.9$ for a width of $\sim 1.1 \pm 0.1$ keV. Moreover, the absorption column density N_H turns out to be $\sim 0.23 \times 10^{22} \text{ cm}^{-2}$ which is similar to the value reported in Zhang et al. (2024). Thus, the final model used to fit the *AstroSat*/LAXPC spectrum

Table 1. Log of the observations used in the analysis along with their exposure time.

Segments	Instruments	Observation Ids	Date of Obs.		Exposure time (s)
			Start MJD	Stop MJD	
HS	NICER	4202130101	59336.149	59336.867	516.00
		4202130102	59337.053	59337.060	535.00
		4202130103	59338.927	59338.995	566.00
		4202130104	59339.056	59339.96	4039.00
HIMS	AstroSat	T04 003T01 9000004368 (A1)	59345.048	59345.499	40000.00
		T04 006T01 9000004370 (A2)	59345.504	59346.725	50000.00
SIMS1	NICER	4202130105	59352.745	59352.951	2680.00
		4202130106	59353.006	59353.925	12211.00
		4202130107	59354.038	59354.501	4631.00
SIMS2	NICER	4202130108	59355.334	59355.868	3809.00
		4202130109	59356.904	59356.496	3020.00
		4675020103	59357.012	59357.938	5372.00
		4202130110	59357.401	59357.227	7508.00
		4202130111	59357.982	59358.058	2456.00
		4675020104	59358.175	59358.391	2671.00
SIMS3	NICER	4202130112	59359.078	59359.941	3683.00
		4675020105	59359.224	59359.475	2535.00
SIMS4	NICER	4675020106	59360.120	59360.459	1867.00
		4642010101	59360.574	59360.967	4318.00
		4642010102	59361.026	59361.225	768.00
HSS	NICER	4675020107	59363.211	59363.991	4926.00
		4202130114	59364.051	59364.443	1749.00
		4675020108	59364.501	59364.960	3574.00
		4675020109	59365.018	59365.993	5859.00
		4202130115	59365.211	59365.670	3912.00
		4675020110	59365.997	59369.942	4791.00

is $\text{Tbabs} \times (\text{ThComp} \times \text{diskbb} + \text{Gaussian})$, with kT_e fixed at 100 keV.

Next, we fitted the 1-10 keV *NICER* spectra with the model combination of $\text{Tbabs} \times \text{ThComp} \times \text{diskbb}$. During fitting, we froze N_H and kT_e at the same value for all segments as for the *AstroSat*/LAXPC case. For HS, this model combination gave a reduced chi-square of 1.47 (207.30/141). We observed a hump in residuals around ~ 6.5 keV, and thereby, we added a **Gaussian** component fixed at 6.5 keV to resolve it, and we obtained the reduced chi-square 0.59 (80.88/139).

For the SIMS1 segment, we fitted the spectrum using $\text{Tbabs} \times \text{ThComp} \times \text{diskbb}$ and obtained a reduced χ^2 of 0.3 (44.64/163). Based on this, we adopted this model as the best-fit configuration and applied it to the remaining segments. It is important to note that the **Gaussian** component was used only for the HIMS (LAXPC) and HS (*NICER*) segments, where significant residuals around 6.5 keV were observed. All other segments were fitted without a Gaussian component. Using the default systematic error from `nicer13-spect`, we obtained reduced χ^2 values in the range of 0.3–0.6 across all *NICER* observations (HS, SIMS1, SIMS2, SIMS3, SIMS4, and HSS). These low reduced χ^2 values for the

NICER segments likely indicate an overestimation of the default systematics. Figure 3 shows the spectrum of all the *NICER* segments fitted using the best-fit model. The residuals observed at energies less than and around 2 keV in Figure 3 (*NICER* segments) could be due to the calibration uncertainty at the Si and Au edges (Rout et al. 2021). In the SIMS2 segment, these instrumental features were more prominent in the residuals, and thus, we modeled them using two **edge** components at 1.8 keV and 2.5 keV.

Table 2 lists the values of best-fit spectral parameters, and Figure 4 shows the evolution of spectral parameters with time for all the *NICER* and *AstroSat* segments (HS, HIMS, HSS, and the four SIMS segments). We have marked each parameter value of different states following the same color code as discussed before.

3.3. Extraction of rms and lag

We computed the rms and time lag energy spectra in 4-30 keV using the subroutine `laxpc_find_freq_lag` at the centroid frequency of the detected QPO for *AstroSat* observation (HIMS) as shown in Figure 5. Similarly, we computed the rms and lag spectra in 1-10 keV us-

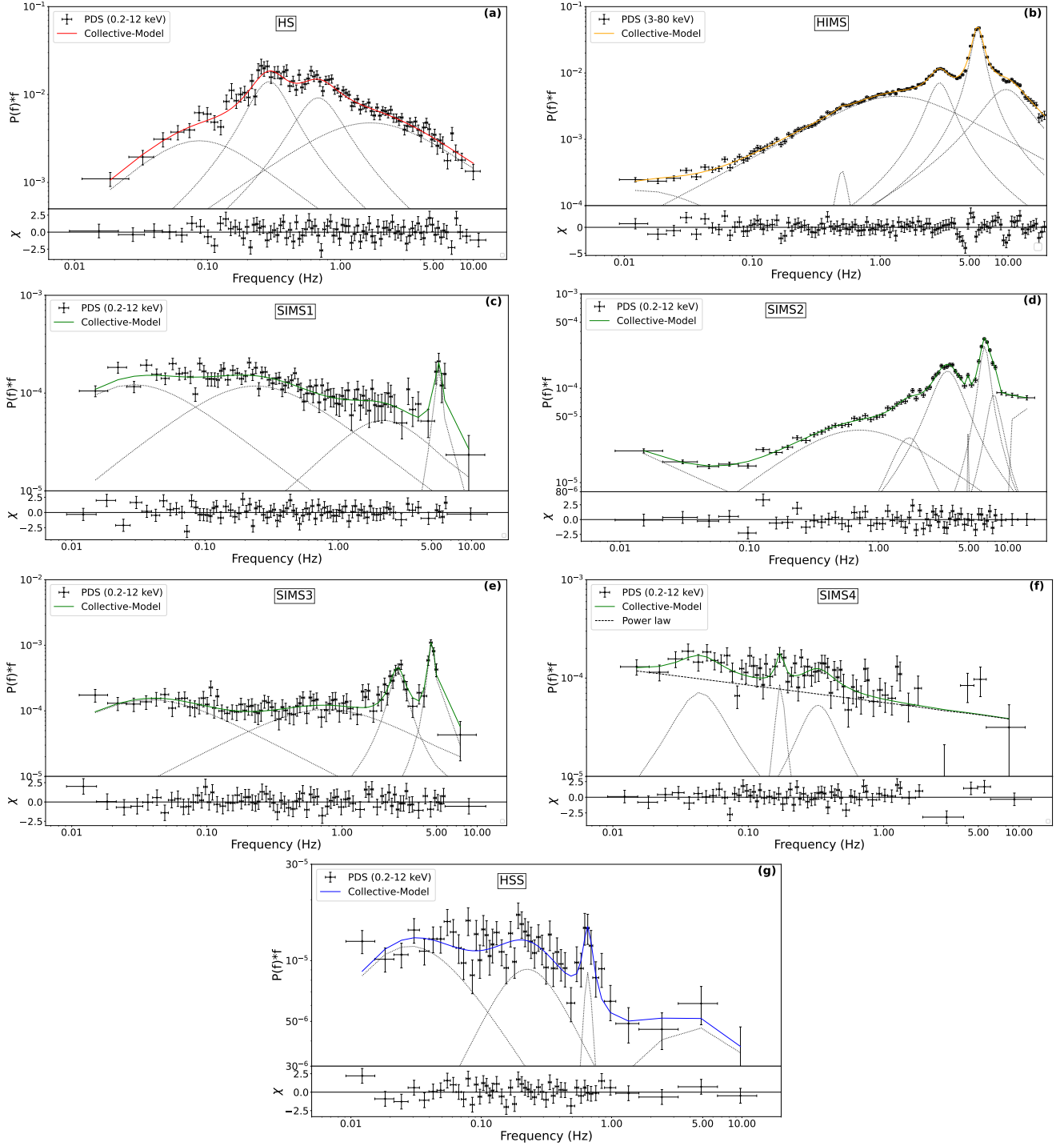


Figure 2. Power Density Spectra (PDS) of all segments in the 0.005–20 Hz frequency range. Each panel shows the PDS of an individual segment fitted with multiple Lorentzian components, along with the corresponding residuals from the best-fit model.

ing `nicer_find_freqflag` for all four SIMS segments as shown in Figure 5.

Both the subroutine estimates the rms and lag for different energy bins in particular energy range (for *AstroSat* (4–30 keV) and for *NICER* (1–10 keV)) using inputs like frequency resolution Δf (equal to or half

of FWHM (full width at half maximum) of QPO frequency) and QPO frequency or the characteristic frequency of the Lorentzian ($\nu = \sqrt{\nu_0^2 + \Delta^2}$, where ν_0 corresponds to centroid frequency and Δ is the half-width at half-maximum (HWHM= $\sigma/2$)). The rms is calculated as the square root of the integration of the power

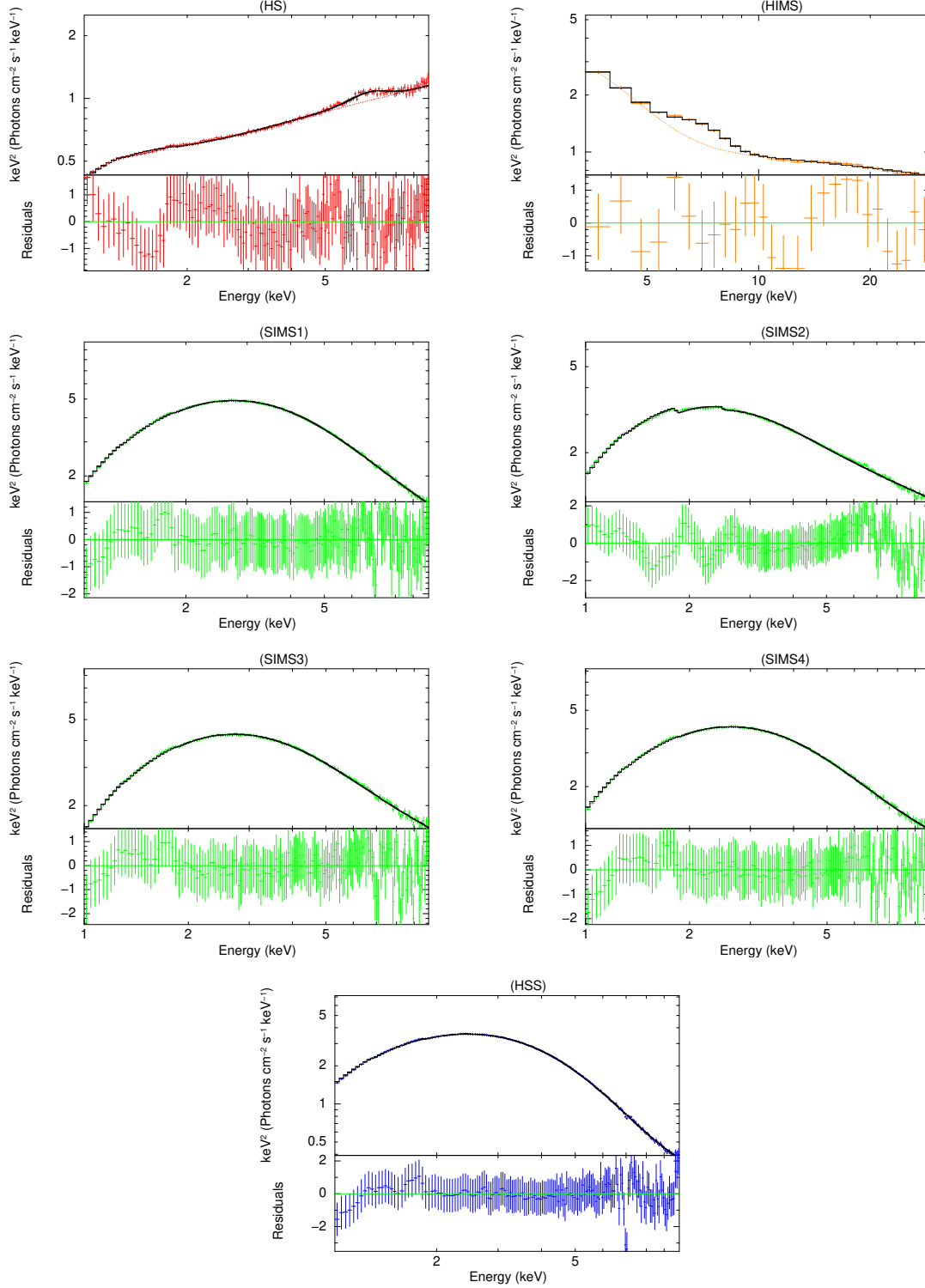


Figure 3. Photon spectra of different spectral states. *NICER* segments HS, SIMS1, SIMS2, SIMS3, SIMS4, and HSS are in the 1-10 keV energy range, while *AstroSat*/LAXPC (HIMS) is in the 3-30 keV energy range. The model used is `constant` \times `Tbabs` \times `ThComp` \times `diskbb`, where kT_e is fixed at 100 keV. For HS and HIMS, we have added a `Gaussian` component fixed at 6.5 keV.

spectra in the frequency range $f - \Delta f$ and $f + \Delta f$ for a particular band. Along with the rms, phase lag is also

computed by the subroutine for the cross-spectra of the two light curves of different energy bands using one as

Table 2. The best-fit spectral parameters and reduced χ^2 of different segments with errors calculated at the 90% confidence level. The value of kT_e is fixed at 100.0 keV for all segments.

SEG	Γ	cov_frac	kT_{in} (keV)	N_{Disk}	χ^2/dof
HS	$1.61^{+0.02}_{-0.02}$	$0.61^{+0.02}_{-0.02}$	$0.29^{+0.01}_{-0.01}$	12600^{+1900}_{-2400}	81.88/139
HIMS	$2.15^{+0.02}_{-0.02}$	$0.27^{+0.03}_{-0.03}$	$0.74^{+0.04}_{-0.04}$	2000^{+550}_{-780}	19.60/22
SIMS1	$3.06^{+0.01}_{-0.05}$	> 0.94	$0.91^{+0.01}_{-0.01}$	1030^{+20}_{-33}	44.64/163
SIMS2	$2.66^{+0.01}_{-0.01}$	> 0.99	$0.66^{+0.01}_{-0.01}$	2530^{+60}_{-60}	99.86/164
SIMS3	$2.79^{+0.01}_{-0.03}$	> 0.96	$0.86^{+0.01}_{-0.01}$	1080^{+30}_{-30}	63.77/155
SIMS4	$2.9^{+0.1}_{-0.1}$	$0.8^{+0.1}_{-0.1}$	$0.88^{+0.01}_{-0.01}$	980^{+50}_{-50}	57.93/155
HSS	$3.1^{+0.2}_{-0.2}$	$0.32^{+0.07}_{-0.06}$	$0.91^{+0.01}_{-0.01}$	800^{+20}_{-20}	73.57/159

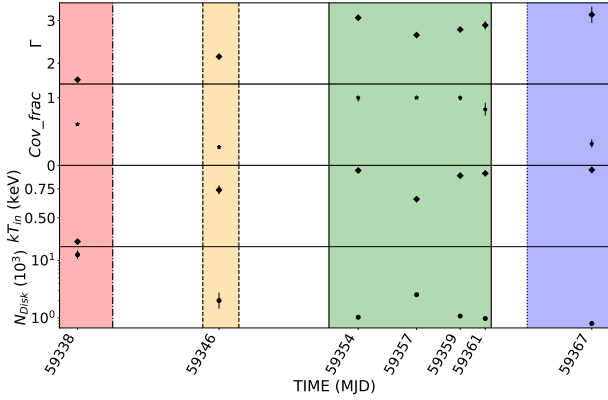


Figure 4. The evolution of spectral parameters with time (MJD). The errors are calculated at the 90% confidence level. The MJDs of various segments were calculated as the mean of the starting and ending timings of distinct observations.

a reference energy band (E_{ref}). This subroutine also uses different inputs, such as the minimum frequency and maximum frequency, or the Nyquist frequency.

We observed that the rms increased with energy for all the segments. However, we found different strengths of fractional variability in different states. In LHS (HS segment), rms for the broad feature is maximum at $\sim 13\%$ in 5-7 keV energy band with a positive time lag, which increased to 114 ms in 5-7 keV but then decreased to 80 ms in 7-10 keV energy band as it can be seen in Figure 5 (HS). The average fractional variability in the HIMS segment is $\sim 6\%$ in the 4-30 keV band. The average fractional variability in different segments of SIMS is between 2% and 23% over the full energy band (1-10 keV). The HIMS segment showed negative lags (soft lags), which decreased monotonically over the full en-

ergy range till ~ 5 ms Figure 5. We observed that the nature of the time lags shifted to negative in SIMS3 with a maximum negative lag of 50 ms for the energy band 6-10 keV, while for SIMS1, SIMS2, and SIMS4, we observed the positive nature of the lag with the average positive lag in the range between ~ 5 ms and ~ 66 ms, as shown in Figure 5. We found insignificant variations in the fractional variability and time lag during the HS segment.

3.4. Modelling the rms and time lag spectra

Next, we modeled the energy-dependent rms and time lag computed at different frequencies of QPOs and aperiodic bumps detected in HS, HIMS, and the four SIMS segments. We used the technique given by Garg et al. (2020), which models the energy-dependent temporal properties using the spectral information of the source. This model considers an accretion flow consisting of a geometrically thin and optically thick disk truncated at some radius far from ISCO and a hot, optically thin, and geometrically thick corona consisting of high-energy electrons near the BH. Garg et al. (2020) models both outer truncated disk and coronal emissions using the XSPEC components `diskbb` and `ThComp`, respectively. In their model, they also translated the spectral parameter kT_e into a more physical parameter, heating rate (\dot{H}) for the analysis. So, there are five parameters kT_{in} , τ , \dot{H} , f_{sc} (equivalent to parameter cov_frac), and N_{disk} which are obtained by fitting the time-averaged photon spectrum. According to Garg et al. (2020), the variations on the spectral parameters can cause the variation

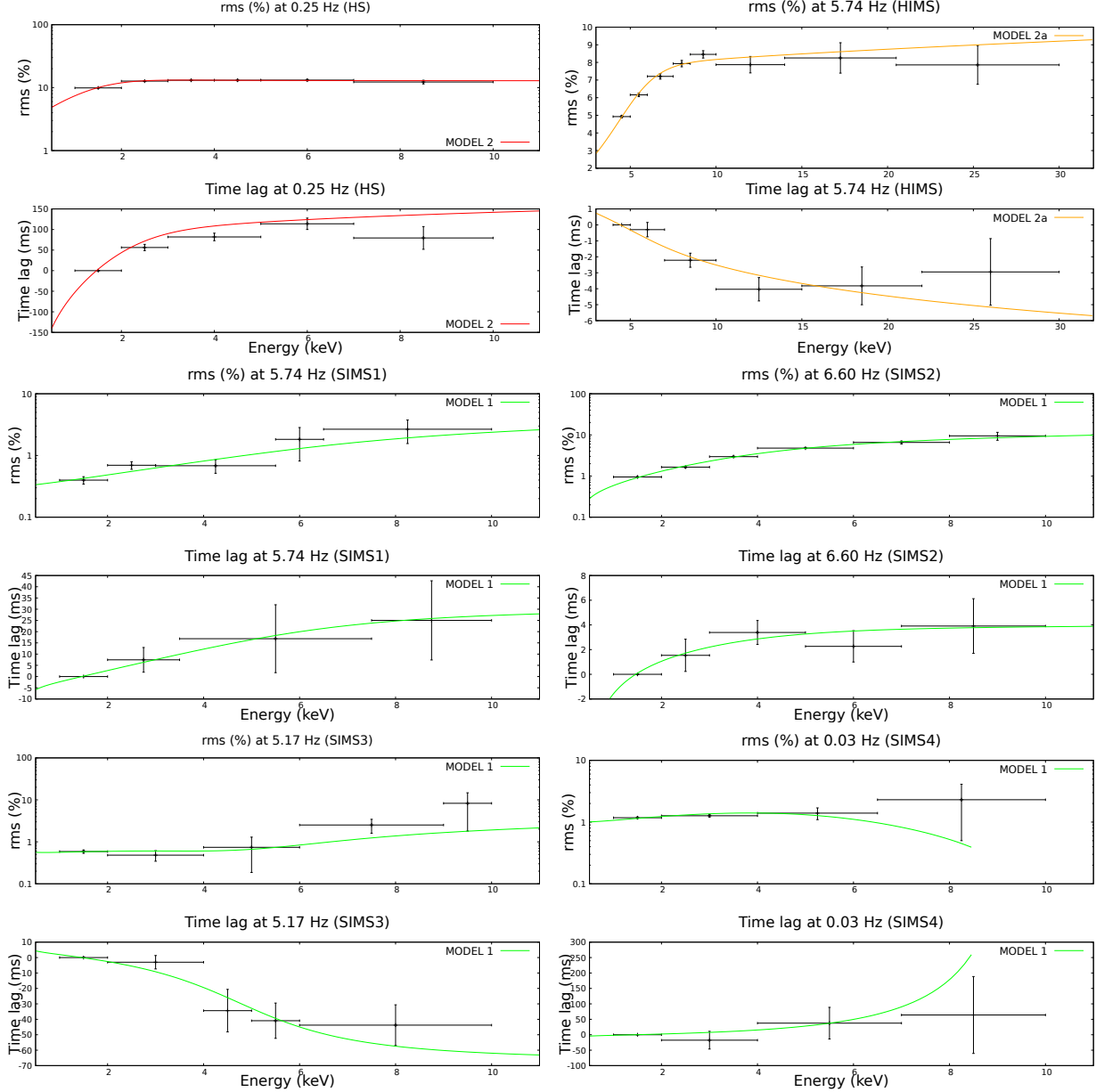


Figure 5. The observed rms and time lag in various segments fitted with different models. The plots illustrate different segment number, along with the peak frequency at which rms and time lag are determined. The fitted model for the observed rms and lag are also indicated within the plot. The parameter values of the model are given in Table 3.

in the steady state spectrum ($F(E)$) given as

$$\Delta F(E) = \sum_{j=1}^M \frac{\partial F(E)}{\partial \alpha_j} \Delta \alpha_j \quad (1)$$

where α_j are the spectral parameters and the small variations of these parameter values are denoted by $\Delta \alpha_j$, and M is the number of parameters. $\Delta \alpha_j$ can be written as $A_j \exp(i\omega_j t)$, A_j is the amplitude, and ω_j denotes the frequency of sinusoidal variations. They estimated rms using $(\frac{1}{\sqrt{2}})|\Delta F(E)|/F(E)$ and phase lag using the argument of $\Delta F(E_{ref}) \times \Delta F(E)$, where E_{ref} is the ref-

erence energy band. The phase lag can be easily calculated as the product of the time lag and $2\pi\nu$ where ν is the frequency of the signal.

The heating rate (\dot{H}) of the corona can be defined as the energy difference between the emitted Comptonized spectrum and the incoming seed photon flux. Mathematically, it can be defined by equation 2.

$$\dot{H} = \int E(F_c(E, kT_e, \tau) - F_{inp}(E))dE \quad (2)$$

where F_c is the photon flux from the corona and $F_{inp}(E) = f * F_d$ is the seed photon flux.

The predicted rms and lag can then be compared with the observed energy-dependent rms and lag spectra. Further, Garg et al. (2022) converted the parameters δN_{disk} and δkT_{in} into δR_{in} and $\delta \dot{M}$ respectively, using the relations $R_{in} \propto N_{disk}^{1/2}$ and $\dot{M} \propto T_{in}^4 R_{in}^3$. Thereby, they fitted the rms and lag spectra using the variations in \dot{M} , τ , \dot{H} , f_{sc} , and R_{in} .

First, we modeled the rms and lag spectra at Type-C QPO frequency detected in the HIMS segment. Following Garg et al. (2022), we first fitted a simple MODEL 1, which consisted of variations in the accretion rate ($\delta \dot{M}$) and the heating rate ($\delta \dot{H}$) along with a phase delay between them. The fitting gave a reduced χ^2 of > 2 . Next, we introduced variation in f_{sc} with some phase delay ($\phi_{f_{sc}}$) with respect to the accretion rate, and we obtained a good fit with a reduced χ^2 of ~ 1.43 (11.42/8). We call this model MODEL 2. However, we found that $\phi_{f_{sc}}$ was consistent with zero during the fitting, and therefore fixed it to zero, assuming no delay with respect to the accretion rate. By doing this, we obtained χ^2/dof as 11.42/9 ~ 1.26 . We call this model MODEL 2a. The parameter values of the fitting of the MODEL 2a on HIMS are given in Table 3.

In Table 3, the parameters expressed in percentage (%) provide an intuitive measure of the relative modulation strength, allowing for a direct comparison of which parameters contribute most to the observed variability. The phase lag values are used to compute the corresponding time lags ($T_{\dot{H}}$ and $T_{f_{sc}}$) between parameter variations, expressed in milliseconds. Depending on the sign and value of the phase lag, as well as the percentage variations in the disk and coronal parameters, one can infer from which parameter the variability originated, the timescale and direction of its propagation, and which parameter began to vary in response to the perturbation. For instance, in the HIMS segment, the rms and lag spectra are fitted using MODEL 2a, which incorporates variations in the accretion rate, coronal heating rate, and scattering fraction, along with the lag w.r.t. the accretion rate. The results suggest that the coronal variations are due to the variations in both the heating rate and scattering fraction parameters. Moreover, the negative lags indicate that the coronal variations lead the accretion rate, implying an outward propagation of perturbations from the corona to the disk.

Further, we fitted the rms and lag spectra for Type-B QPOs detected in SIMS's segments (SIMS1, SIMS2 and SIMS3). We first fitted the rms and lag of SIMS1 with the same MODEL 1 as previously and obtained a reduced χ^2 of ~ 0.92 as shown in Figure 5. Next, we found that reduced χ^2 varies from 0.89 to 1.19 for SIMS1, SIMS2, and SIMS3 segments, indicating that

MODEL 1 is a good fit for the observed rms and lag spectra. We refrained from further fitting with other models so as not to overfit the data. Further, we fitted the rms and lag spectra for the broad feature seen for SIMS4 with MODEL 1 and obtained a good fit with reduced χ^2 of ~ 1.11 . Table 3 lists all three best-fit parameters and reduced χ^2 for all SIMS segments.

Lastly, we modeled the rms and time lag of the aperiodic hump observed in the power spectra of the HS segment. We found that MODEL 1 can't fit the observed rms and lags. So, we tried with MODEL 2 and got a fit of a reduced χ^2 of ~ 0.66 . The parameter values of the fit are given in Table 3. We restrain further variation in parameters to avoid overfitting. Lastly, we found insignificant variations for HSS in the soft state and refrained from modeling its rms and lag spectra.

4. DISCUSSION AND CONCLUSIONS

We performed the spectral and timing study of MAXIJ1803 using *AstroSat* and *NICER* observations. We used the month-long observations of the source during its 2021 outburst as it transited through LHS, HIMS, SIMS, and HSS. It became quite favorable that *NICER*, which works in 0.2-12 keV, captured the source during the SIMS and HSS, which are dominated predominantly by soft emission. Additionally, *NICER* also observed the source during LHS, capturing the hard emission in soft energy bands. Similarly, *AstroSat*/LAXPC, which works in 3-80 keV, observed the source during HIMS. We could perform the spectral and temporal analysis for all the spectral states of the source.

The MAXI light curve, along with hardness variations (Figure 1 (a) and (b)) and the HID plot (Figure 1 (c)), show the rise and decline of the source through the outburst. Though the MAXI count rates show the expected behavior for all the states, hardness variations seem to drop from a high value for LHS to a smaller value, which stayed constant during HIMS, SIMS, and HSS. Further, the source trajectory in the HID doesn't completely resemble but is somewhat like a 'Q' pattern as expected for BHXBs (Belloni et al. 2005a). The radio observations taken from Wood et al. (2023) are marked as stars in HID to distinguish among spectral states as provided by Wood et al. (2023) (in Table 1). We further confirmed this using our spectral and temporal analysis.

Our spectral analysis revealed that the source emission in all the states can be described as the blackbody emission from an outer thermal disk and the Comptonized emission from the coronal region. Interestingly, the parameter evolutions obtained in our spectral states also suggest the spectral transitions across different spectral states. Moreover, we found a low inner disk tempera-

Table 3. The physical parameters of various models in different segments where errors are calculated at 1σ level.

Frequency (Hz)	SEG	Model	$ \delta\dot{M} $ (%)	$ \delta\dot{H} $ (%)	$\phi_{\dot{H}}$	$T_{\dot{H}}$ (ms)	$ \delta f_{sc} $ (%)	$\phi_{f_{sc}}$	$T_{f_{sc}}$ (ms)	χ^2/dof
0.25	HS	MODEL 2	$9.3^{+0.9}_{-0.9}$	$15.6^{+3.9}_{-3.9}$	$0.4^{+0.2}_{-0.2}$	264^{+120}_{-110}	$9.9^{+2.1}_{-2.1}$	$0.47^{+0.22}_{-0.22}$	300^{+140}_{-140}	3.30/5
5.74	HIMS	MODEL 2a	$1.9^{+0.2}_{-0.2}$	$12.7^{+0.6}_{-0.6}$	$-0.20^{+0.03}_{-0.03}$	$-5.6^{+0.7}_{-0.7}$	$8.6^{+1.0}_{-1.0}$	—	—	11.42/9
5.74	SIMS1	MODEL 1	$0.7^{+0.1}_{-0.1}$	$3.4^{+1.1}_{-1.1}$	$1^{+0.4}_{-0.4}$	28^{+12}_{-11}	—	—	—	4.43/5
6.60	SIMS2	MODEL 1	$1.25^{+0.05}_{-0.05}$	$10.9^{+0.3}_{-0.3}$	$0.17^{+0.04}_{-0.04}$	$4.2^{+1.0}_{-1.0}$	—	—	—	6.44/7
5.17	SIMS3	MODEL 1	$0.9^{+0.1}_{-0.1}$	4^{+1}_{-1}	$-2.1^{+0.3}_{-0.4}$	-64^{+10}_{-11}	—	—	—	7.17/6
0.03	SIMS4	MODEL 1	$1.8^{+0.05}_{-0.05}$	$0.9^{+0.7}_{-0.2}$	< 1.2	< 6250	—	—	—	4.44/4

ture and a high disk normalization, which indicates the presence of a cold disk being truncated at a large distance from the BH and coronal regions dominating the X-ray emission, which is a typical feature of a low-hard state (Narayan & Yi 1995; Liu et al. 2007).

We also detected a Gaussian line emission in the HS segment, peaking around ~ 6.5 keV with $\sigma \sim 0.9^{+0.2}_{-0.2}$ and norm $\sim 0.005^{+0.002}_{-0.001}$. The presence of narrow or broad reflection line components in the hard state spectra has previously been reported in sources like Cyg X-1 (Parker et al. 2015) and MAXI J1820+070 (Kara et al. 2019; Buisson et al. 2019). The HS often consists of compact jets with a spectrum ranging from radio wavelength to near-IR wavelength (Gandhi et al. 2011), which likely extends to X-rays and γ -rays. The compact jets can emit X-rays from different heights, illuminating both the inside and outside of the truncated disk, leading to reflection features in the hard state (Kara et al. 2019; Buisson et al. 2019).

Next, as the source moved to the HIMS segment, there was a large decrease in the disk normalization and an increase in the inner disk temperature, indicating that the source transited to the HIMS. Further, as the source moves through the four SIMS segments, the kT_{in} continues to increase with disk normalization becoming very small. Collectively, it shows that the truncated disk has advanced towards the BH, and thereby, the emitted flux is getting softer, which is often seen for SIMS and HSS (Belloni et al. 2011). Our results are consistent with the findings of Wood et al. (2023), which used radio observations as discussed in Section 2.2. We also found an absorption feature in the residuals of our spectrum in all four SIMS segments and in HSS but we refrain from modeling it with **Gaussian**, as the reduced χ^2 values are overestimated due to the default systematics of the **nicer13-spect**. Zhang et al. (2024) also reported such absorption features in MAXIJ1803 in different epochs of SIMS and HSS, indicating the presence of winds.

Our temporal analysis showed that the power spectrum for LHS possesses broad features, but as the

source transited to HIMS, Type-C QPOs along with sub-harmonic appeared at the frequencies of $\sim 5.75 \pm 0.08$ Hz and 1.16 ± 0.06 Hz respectively. Further, as the source shifted to SIMS, Type-C QPOs disappeared, with Type-B QPOs appearing in the PDS within the range ~ 5.17 -6.61 Hz. We confirmed the types of QPOs using the quality factor (Q: $\nu_{\text{centroid}}/FWHM$), rms (%), and the detection of QPOs in different spectral states. The QPO, detected in the HIMS segment, have the Q factor of ~ 5 and the rms (%) of $\sim 12\%$, indicating that they are type C. The Q-factor of ~ 5 -10, rms of ~ 0.63 -2.84%, and detection in SIMS (Belloni et al. 2005b) using **NICER** segments, indicated type-B QPOs. Similar values of Q and rms (%) have been reported by Chand et al. (2022); Jana et al. (2022); Zhu et al. (2023). Lastly, in the HSS, the variability is quite low, with only broad features seen in the PDS. Further, we couldn't detect any sharp correlations between the QPO frequency and spectral parameters over the source evolution.

We modeled the observed behavior of energy-dependent fractional rms and time lag using the technique devised by Garg et al. (2020). For the Type-C QPOs detected in the HIMS segment, we discovered that the dynamic origin of the QPO is from the corona, which propagated away from the BH, causing perturbations in f_{sc} without any time delay, which further caused variation in the accretion rate.

For Type-B QPOs detected during SIMS (SIMS1, SIMS2, and SIMS3 segment), we found that the variations in coronal heating rate and accretion rate, along with a time delay, can explain the observed temporal features of QPOs. However, as the observed time lags swung between positive and negative, the modeled phase lag also came out to be changing between positive and negative. The associated time delays are greater than those for Type-C QPOs. This could be due to corona contraction or a change in the orientation of the corona from horizontal to vertical (Ma et al. 2023). We also found that this same model can describe the observed rms and lag for an aperiodic hump in SIMS4, suggesting

Table 4. The table gives information about the inferences made by modeling the rms and time lag of different variability features observed during different spectral states.

Spectral states	Type of variability feature	Nature of lag	Initial Variation	Variation after a time delay
LHS (HS segment)	Broad feature	Positive lag	Accretion rate	Coronal heating rate and fractional scattering
HIMS (HIMS segment)	Type-C QPO	Negative lag	Coronal heating rate	Accretion rate and fractional scattering
SIMS (SIMS1 and SIMS2 segment)	Type-B QPO	Positive lag	Accretion rate	Coronal heating rate
SIMS (SIMS3 segment)	Type-B QPO	Negative lag	Coronal heating rate	Accretion rate
SIMS (SIMS4 segment)	Broad feature	Positive lag	Accretion rate	Coronal heating rate
HSS (HSS segment)	-	-	-	-

that the same combination of variations can give rise to aperiodic humps also.

Lastly, for the HS segment, we required variations in \dot{M} , \dot{H} , and f_{sc} along with some phase delays between them to describe the observed temporal features. Table 3 gives information about the variations required to describe different variability features. We note here that the nature of lag for this particular source kept swinging between positive and negative between different spectral states as well. It can imply a continuous change in the dynamic origin of Type-B QPOs between the disk and corona. This was also observed by Garg et al. (2022) for just Type-C QPOs in MAXI J1535-571 during its HIMS and thereby pointed to an underlying resonant phenomenon giving rise to different origins of variability, but there could be some complex scenarios.

Moreover, the time lags for all segments are in the range of ms, which is significantly smaller than the time scale of viscous or mass inflows. Misra et al. (2020) suggested that there could be a propagation of sound waves over ms scales and can give rise to variability in X-ray binaries. It is thereby possible that the perturbation travels from the disk to the corona over sound scales and gives rise to hard lags whereas the perturbations travel from the corona to the disk over a light travel time scales. However, our conclusions are based on the model fitted with the energy-dependent rms and time lag of this particular source hence it cannot be generalized. The approach applied here has the advantage of

getting information on distinctive radiative components responsible for the variation leading to the rise of QPOs.

5. ACKNOWLEDGEMENT

We would like express our gratitude to the High Energy Astrophysics Science Archive Research Centre (HEASARC) for providing the software and data utilised in this project. We are grateful to the LAXPC Payload Operation Center (POC) at IUCAA, Pune, the SXT POC at TIFR, Mumbai, and XRT/NICER for providing the data, the necessary tools, and the analysis guidelines. This research has made use of the MAXI data provided by RIKEN, JAXA and the MAXI team. A.P. and B.S. acknowledge the hospitality and facilities provided by the Inter-University Centre for Astronomy and Astrophysics (IUCAA), Pune, where part of this work was carried out. B.S. would also like to acknowledge the IUCAA visiting associateship program. We thank the anonymous referee for the insightful comments and suggestions.

6. DATA AVAILABILITY

The archived data utilized in this project are available at Astrosat-ISSDC website (http://astrobrowse.issdc.gov.in/astro_archive/archive) and at the NASA's HEASARC website (<https://heasarc.gsfc.nasa.gov/cgi-bin/W3Browse/w3browse.pl>).

APPENDIX

A. PDS PARAMETERS.

From Figure 2, it can be seen that the sub-harmonic, fundamental, and harmonic frequencies are not detected in all segments. We have provided details of all the Lorentzian components used to model the power spectra in Table A1. Additionally, in Table A1, we have highlighted the sub-harmonic frequencies (when detected) in blue at f_3 (Hz), and the fundamental frequencies (or broad components in the HS and SIMS4 segment), used to calculate the rms and lag in red at f_2 (Hz).

REFERENCES

- Adegoke, O. K., García, J. A., Connors, R. M. T., et al. 2024, *ApJ*, 977, 26, doi: [10.3847/1538-4357/ad82e9](https://doi.org/10.3847/1538-4357/ad82e9)
- Agrawal, P. C. 2006, *Advances in Space Research*, 38, 2989, doi: [10.1016/j.asr.2006.03.038](https://doi.org/10.1016/j.asr.2006.03.038)
- Altamirano, D., & Belloni, T. 2012, *ApJL*, 747, L4, doi: [10.1088/2041-8205/747/1/L4](https://doi.org/10.1088/2041-8205/747/1/L4)
- Antia, H. M., Yadav, J. S., Agrawal, P. C., et al. 2017, *ApJS*, 231, 10, doi: [10.3847/1538-4365/aa7a0e](https://doi.org/10.3847/1538-4365/aa7a0e)
- Arzoumanian, Z., Gendreau, K., Baker, C., et al. 2014, in *Space Telescopes and Instrumentation 2014: Ultraviolet to Gamma Ray*, Vol. 9144, SPIE, 579–587
- Bellavita, C., García, F., Méndez, M., & Karpouzas, K. 2022, *MNRAS*, 515, 2099, doi: [10.1093/mnras/stac1922](https://doi.org/10.1093/mnras/stac1922)
- Belloni, T., Homan, J., Casella, P., et al. 2005a, *A&A*, 440, 207, doi: [10.1051/0004-6361:20042457](https://doi.org/10.1051/0004-6361:20042457)
- . 2005b, *A&A*, 440, 207, doi: [10.1051/0004-6361:20042457](https://doi.org/10.1051/0004-6361:20042457)
- Belloni, T. M., & Altamirano, D. 2013, *MNRAS*, 432, 10, doi: [10.1093/mnras/stt500](https://doi.org/10.1093/mnras/stt500)
- Belloni, T. M., & Motta, S. E. 2016, in *Astrophysics and Space Science Library*, Vol. 440, *Astrophysics of Black Holes: From Fundamental Aspects to Latest Developments*, ed. C. Bambi, 61, doi: [10.1007/978-3-662-52859-4_2](https://doi.org/10.1007/978-3-662-52859-4_2)
- Belloni, T. M., Motta, S. E., & Muñoz-Darias, T. 2011, *Bulletin of the Astronomical Society of India*, 39, 409, doi: [10.48550/arXiv.1109.3388](https://doi.org/10.48550/arXiv.1109.3388)
- Bhattacharyya, S., Singh, K. P., Stewart, G., et al. 2021, *Journal of Astrophysics and Astronomy*, 42, 17, doi: [10.1007/s12036-020-09678-z](https://doi.org/10.1007/s12036-020-09678-z)
- Bhattacharjee, S., Nath, A., Sarkar, B., et al. 2024a, *ApJ*, 971, 154, doi: [10.3847/1538-4357/ad583d](https://doi.org/10.3847/1538-4357/ad583d)
- Bhattacharjee, S., Pradhan, A., & Sarkar, B. 2024b, *Physics Frontiers*, Vol-I, 18, doi: [10.48550/arXiv.2409.11721](https://doi.org/10.48550/arXiv.2409.11721)
- Buckley, D. A. H., Brink, J., Charles, P. A., & Groenewald, D. 2021, *The Astronomer’s Telegram*, 14597, 1
- Buisson, D. J. K., Fabian, A. C., Barret, D., et al. 2019, *MNRAS*, 490, 1350, doi: [10.1093/mnras/stz2681](https://doi.org/10.1093/mnras/stz2681)
- Casella, P., Belloni, T., Homan, J., & Stella, L. 2004, *Astronomy & Astrophysics*, 426, 587
- Chakrabarti, S. K., & Manickam, S. G. 2000, *ApJL*, 531, L41, doi: [10.1086/312512](https://doi.org/10.1086/312512)
- Chand, S., Dewangan, G. C., Thakur, P., Tripathi, P., & Agrawal, V. K. 2022, *ApJ*, 933, 69, doi: [10.3847/1538-4357/ac7154](https://doi.org/10.3847/1538-4357/ac7154)
- Coughenour, B. M., Tomsick, J. A., Mastroserio, G., et al. 2023, *ApJ*, 949, 70, doi: [10.3847/1538-4357/acc65c](https://doi.org/10.3847/1538-4357/acc65c)
- Dhaka, R., Misra, R., Jain, P., & Yadav, J. S. 2024, *ApJ*, 974, 90, doi: [10.3847/1538-4357/ad67e4](https://doi.org/10.3847/1538-4357/ad67e4)
- Dhaka, R., Misra, R., Yadav, J. S., & Jain, P. 2023, *MNRAS*, 524, 2721, doi: [10.1093/mnras/stad2075](https://doi.org/10.1093/mnras/stad2075)
- Dunn, R. J. H., Fender, R. P., Körding, E. G., Belloni, T., & Cabanac, C. 2010, *MNRAS*, 403, 61, doi: [10.1111/j.1365-2966.2010.16114.x](https://doi.org/10.1111/j.1365-2966.2010.16114.x)
- Espinasse, M., Carotenuto, F., Tremou, E., et al. 2021, *The Astronomer’s Telegram*, 14607, 1
- Feng, Y., Zhao, X., Li, Y., et al. 2022, *MNRAS*, 516, 2074, doi: [10.1093/mnras/stac1868](https://doi.org/10.1093/mnras/stac1868)
- Gandhi, P., Blain, A. W., Russell, D. M., et al. 2011, *ApJL*, 740, L13, doi: [10.1088/2041-8205/740/1/L13](https://doi.org/10.1088/2041-8205/740/1/L13)
- García, F., Karpouzas, K., Méndez, M., et al. 2022, *MNRAS*, 513, 4196, doi: [10.1093/mnras/stac1202](https://doi.org/10.1093/mnras/stac1202)
- Garg, A., Misra, R., & Sen, S. 2020, *MNRAS*, 498, 2757, doi: [10.1093/mnras/staa2506](https://doi.org/10.1093/mnras/staa2506)
- . 2022, *MNRAS*, 514, 3285, doi: [10.1093/mnras/stac1490](https://doi.org/10.1093/mnras/stac1490)
- Gendreau, K., & Arzoumanian, Z. 2017, *Nature Astronomy*, 1, 895, doi: [10.1038/s41550-017-0301-3](https://doi.org/10.1038/s41550-017-0301-3)
- Gendreau, K. C., Arzoumanian, Z., Adkins, P. W., et al. 2016, in *Space telescopes and instrumentation 2016: Ultraviolet to gamma ray*, Vol. 9905, SPIE, 420–435
- Gropp, J. D., Kennea, J. A., Lien, A. Y., et al. 2021, *The Astronomer’s Telegram*, 14591, 1
- Homan, J., & Belloni, T. 2005, *Ap&SS*, 300, 107, doi: [10.1007/s10509-005-1197-4](https://doi.org/10.1007/s10509-005-1197-4)

Table A1. Best-fitting Lorentzian parameters of the PDS for all segments.

Components	HS	HIMS	SIMS1	SIMS2	SIMS3	SIMS4	HSS
f_1 (Hz)	0.0*	0.0*	0.0*	0.0*	0.0*	-	0.0*
σ_1	$3.4^{+1.0}_{-0.7}$	$0.02^{+0.01}_{-0.01}$	$0.05^{+0.02}_{-0.01}$	$1.4^{+0.3}_{-0.2}$	$0.07^{+0.02}_{-0.02}$	-	$0.06^{+0.02}_{-0.03}$
N_{L1} (10^{-3})	$15.0^{+4.0}_{-4.0}$	$0.5^{+0.1}_{-0.1}$	$0.4^{+0.1}_{-0.1}$	$1.1^{+0.1}_{-0.1}$	$0.5^{+0.1}_{-0.1}$	-	$0.37^{+0.05}_{-0.09}$
f_2 (Hz)	$0.25^{+0.02}_{-0.02}$	$5.74^{+0.02}_{-0.02}$	$5.7^{+0.3}_{-0.2}$	$6.6^{+0.1}_{-0.2}$	$5.17^{+0.05}_{-0.05}$	$0.03^{+0.01}_{-0.03}$	-
σ_2	$0.20^{+0.09}_{-0.07}$	$1.2^{+0.1}_{-0.1}$	$0.7^{+1.0}_{-0.5}$	$1.3^{+0.3}_{-0.7}$	$0.5^{+0.1}_{-0.1}$	$0.03^{+0.04}_{-0.02}$	-
N_{L2} (10^{-3})	20^{+10}_{-10}	$14.0^{+0.1}_{-0.1}$	$0.04^{+0.03}_{-0.02}$	$0.9^{+0.2}_{-0.7}$	$0.18^{+0.03}_{-0.03}$	$0.09^{+0.18}_{-0.07}$	-
f_3 (Hz)	-	$2.84^{+0.04}_{-0.04}$	-	$3.26^{+0.06}_{-0.06}$	$2.8^{+0.1}_{-0.1}$	-	-
σ_3	-	$1.2^{+0.2}_{-0.1}$	-	$2.1^{+0.2}_{-0.2}$	$0.8^{+0.3}_{-0.2}$	-	-
N_{L3} (10^{-3})	-	$4.0^{+1.0}_{-1.0}$	-	$1.4^{+0.1}_{-0.1}$	$0.16^{+0.05}_{-0.04}$	-	-
f_4 (Hz)	$0.59^{+0.08}_{-0.10}$	$0.31^{+0.07}_{-0.10}$	$0.06^{+0.09}_{-0.06}$	$7.9^{+0.4}_{-1.0}$	0.0*	$0.16^{+0.01}_{-0.01}$	$0.14^{+0.07}_{-0.14}$
σ_4	$0.6^{+0.2}_{-0.2}$	$2.6^{+0.3}_{-0.3}$	$0.41^{+0.12}_{-0.06}$	$1.8^{+1.2}_{-0.9}$	$1.6^{+0.7}_{-0.5}$	$0.02^{+0.04}_{-0.02}$	$0.4^{+0.2}_{-0.1}$
N_{L4} (10^{-3})	$11.0^{+6.0}_{-4.0}$	$13.0^{+1.0}_{-1.0}$	$0.3^{+0.1}_{-0.1}$	$0.3^{+0.7}_{-0.2}$	$0.3^{+0.1}_{-0.1}$	$0.02^{+0.02}_{-0.01}$	$0.2^{+0.1}_{-0.1}$
f_5 (Hz)	$0.02^{+0.02}_{-0.02}$	$8.8^{+0.4}_{-0.5}$	$0.5^{+1.2}_{-0.5}$	$1.6^{+0.1}_{-0.1}$	-	$0.29^{+0.05}_{-0.29}$	$0.65^{+0.03}_{-0.02}$
σ_5	$0.14^{+0.13}_{-0.07}$	$7.8^{+0.7}_{-0.6}$	$3.7^{+2.4}_{-1.4}$	$1.0^{+0.7}_{-0.4}$	-	$0.2^{+0.4}_{-0.1}$	$0.12^{+0.17}_{-0.08}$
N_{L5} (10^{-3})	$8.0^{+7.0}_{-4.0}$	$6.0^{+1.0}_{-1.0}$	$0.2^{+0.1}_{-0.1}$	$0.2^{+0.2}_{-0.1}$	-	$0.05^{+0.13}_{-0.03}$	$0.03^{+0.02}_{-0.01}$
f_6 (Hz)	-	$0.50^{+0.03}_{-0.06}$	-	$12.0^{+0.7}_{-0.4}$	-	-	0.0*
σ_6	-	$0.1^{+0.2}_{-0.1}$	-	$0.03^{+16}_{-0.02}$	-	-	$8.1^{+10}_{-4.0}$
N_{L6} (10^{-3})	-	$0.1^{+0.2}_{-0.1}$	-	$0.28^{+0.03}_{-0.04}$	-	-	$0.15^{+0.05}_{-0.05}$
PL_{Index}	-	-	-	$1.6^{+0.1}_{-0.1}$	-	$1.2^{+0.1}_{-0.1}$	-
PL_{norm} (10^{-3})	-	-	-	$0.02^{+0.01}_{-0.01}$	-	$0.06^{+0.01}_{-0.02}$	-
χ^2/dof	93.77/76	141.85/97	80.11/68	70.82/40	44.69/63	64.59/48	50/40

Note: * denotes a fixed parameter during the fitting. f_2 (Hz) shows the QPO/peak frequency component which is used to calculate rms/lag, f_3 (Hz) is the sub harmonic component of the QPO present in HIMS, SIMS2 and SIMS3. σ_{1-6} and N_{L1-6} represents the Lorentzian widths, and their normalizations receptively. PL_{Index} and PL_{norm} represents the components of power law used in fitting broad feature in SIMS2 and SIMS4.

- Homan, J., Wijnands, R., van der Klis, M., et al. 2001, *The Astrophysical Journal Supplement Series*, 132, 377
- Homan, J., Gendreau, K. C., Sanna, A., et al. 2021, *The Astronomer's Telegram*, 14606, 1
- Hosokawa, R., Murata, K. L., Niwano, M., et al. 2021, *The Astronomer's Telegram*, 14594, 1
- Husain, N., Garg, A., Misra, R., & Sen, S. 2023, *MNRAS*, 525, 4515, doi: [10.1093/mnras/stad2481](https://doi.org/10.1093/mnras/stad2481)
- Ingram, A., Done, C., & Fragile, P. C. 2009, *Monthly Notices of the Royal Astronomical Society: Letters*, 397, L101
- Jana, A., Naik, S., Jaisawal, G. K., et al. 2022, *Monthly Notices of the Royal Astronomical Society*, 511, 3922–3936, doi: [10.1093/mnras/stac315](https://doi.org/10.1093/mnras/stac315)
- Kara, E., Steiner, J. F., Fabian, A. C., et al. 2019, *Nature*, 565, 198, doi: [10.1038/s41586-018-0803-x](https://doi.org/10.1038/s41586-018-0803-x)
- Karpouzas, K., Méndez, M., García, F., et al. 2021, *MNRAS*, 503, 5522, doi: [10.1093/mnras/stab827](https://doi.org/10.1093/mnras/stab827)
- Karpouzas, K., Méndez, M., Ribeiro, E. M., et al. 2020, *MNRAS*, 492, 1399, doi: [10.1093/mnras/stz3502](https://doi.org/10.1093/mnras/stz3502)
- Kumar, N., & Misra, R. 2014, *MNRAS*, 445, 2818, doi: [10.1093/mnras/stu1946](https://doi.org/10.1093/mnras/stu1946)
- Kylafis, N. D., & Belloni, T. M. 2015, *A&A*, 574, A133, doi: [10.1051/0004-6361/201425106](https://doi.org/10.1051/0004-6361/201425106)
- Laor, A. 1991, *ApJ*, 376, 90, doi: [10.1086/170257](https://doi.org/10.1086/170257)
- Lee, H. C., Misra, R., & Taam, R. E. 2001, *ApJL*, 549, L229, doi: [10.1086/319171](https://doi.org/10.1086/319171)
- Lewin, W. H. G., van Paradijs, J., & van den Heuvel, E. P. J. 1997, *X-ray Binaries*
- Liu, B. F., Taam, R. E., Meyer-Hofmeister, E., & Meyer, F. 2007, *ApJ*, 671, 695, doi: [10.1086/522619](https://doi.org/10.1086/522619)
- Ma, R., Méndez, M., García, F., et al. 2023, *MNRAS*, 525, 854, doi: [10.1093/mnras/stad2284](https://doi.org/10.1093/mnras/stad2284)
- Maqbool, B., Mudambi, S. P., Misra, R., et al. 2019, *MNRAS*, 486, 2964, doi: [10.1093/mnras/stz930](https://doi.org/10.1093/mnras/stz930)
- Mata Sánchez, D., Muñoz-Darias, T., Cúneo, V. A., et al. 2022, *ApJL*, 926, L10, doi: [10.3847/2041-8213/ac502f](https://doi.org/10.3847/2041-8213/ac502f)
- Miller, J. M. 2007, *ARA&A*, 45, 441, doi: [10.1146/annurev.astro.45.051806.110555](https://doi.org/10.1146/annurev.astro.45.051806.110555)
- Mir, M. H., Misra, R., Pahari, M., Iqbal, N., & Ahmad, N. 2016, *Monthly Notices of the Royal Astronomical Society*, 457, 2999
- Misra, R., & Mandal, S. 2013, *The Astrophysical Journal*, 779, 71
- Misra, R., Rawat, D., Yadav, J. S., & Jain, P. 2020, *ApJL*, 889, L36, doi: [10.3847/2041-8213/ab6ddc](https://doi.org/10.3847/2041-8213/ab6ddc)
- Misra, R., Yadav, J. S., Verdhhan Chauhan, J., et al. 2017, *ApJ*, 835, 195, doi: [10.3847/1538-4357/835/2/195](https://doi.org/10.3847/1538-4357/835/2/195)
- Mitsuda, K., Inoue, H., Koyama, K., et al. 1984, *PASJ*, 36, 741
- Mitsuda, K., Inoue, H., Koyama, K., et al. 1984, *Astronomical Society of Japan, Publications* (ISSN 0004-6264), vol. 36, no. 4, 1984, p. 741-759., 36, 741
- Miyamoto, S., Kitamoto, S., Hayashida, K., & Egoshi, W. 1995, *ApJL*, 442, L13, doi: [10.1086/187804](https://doi.org/10.1086/187804)
- Molteni, D., Tóth, G., & Kuznetsov, O. A. 1999, *ApJ*, 516, 411, doi: [10.1086/307079](https://doi.org/10.1086/307079)
- Motta, S. E. 2016, *Astronomische Nachrichten*, 337, 398, doi: [10.1002/asna.201612320](https://doi.org/10.1002/asna.201612320)
- Nandi, A., Debnath, D., Mandal, S., & Chakrabarti, S. K. 2012, *A&A*, 542, A56, doi: [10.1051/0004-6361/201117844](https://doi.org/10.1051/0004-6361/201117844)
- Narayan, R., & Yi, I. 1995, *ApJ*, 452, 710, doi: [10.1086/176343](https://doi.org/10.1086/176343)
- Parker, M. L., Tomsick, J. A., Miller, J. M., et al. 2015, *ApJ*, 808, 9, doi: [10.1088/0004-637X/808/1/9](https://doi.org/10.1088/0004-637X/808/1/9)
- Rout, S. K., Méndez, M., Belloni, T. M., & Vadawale, S. 2021, *MNRAS*, 505, 1213, doi: [10.1093/mnras/stab1341](https://doi.org/10.1093/mnras/stab1341)
- Serino, M., Negoro, H., Nakajima, M., et al. 2021, *The Astronomer's Telegram*, 14587, 1
- Shidatsu, M., Kobayashi, K., Negoro, H., et al. 2022, *ApJ*, 927, 151, doi: [10.3847/1538-4357/ac517b](https://doi.org/10.3847/1538-4357/ac517b)
- Singh, K. P. 2022, in *Handbook of X-ray and Gamma-ray Astrophysics*, 83, doi: [10.1007/978-981-16-4544-0_31-1](https://doi.org/10.1007/978-981-16-4544-0_31-1)
- Singh, K. P., Stewart, G. C., Westergaard, N. J., et al. 2017, *Journal of Astrophysics and Astronomy*, 38, 29, doi: [10.1007/s12036-017-9448-7](https://doi.org/10.1007/s12036-017-9448-7)
- Singh, K. P., Girish, V., Tiwari, J., et al. 2021, *Journal of Astrophysics and Astronomy*, 42, 83, doi: [10.1007/s12036-021-09756-w](https://doi.org/10.1007/s12036-021-09756-w)
- Steiner, J. F., Ubach, S., Tomsick, J. A., Coughenour, B., & Homan, J. 2021, *The Astronomer's Telegram*, 14994, 1
- Stella, L., Vietri, M., & Morsink, S. M. 1999, *The Astrophysical Journal*, 524, L63
- Sunyaev, R. A., & Titarchuk, L. G. 1980, *A&A*, 86, 121
- Tanenia, H., Garg, A., Misra, R., & Sen, S. 2024, *ApJ*, 975, 190, doi: [10.3847/1538-4357/ad7d8b](https://doi.org/10.3847/1538-4357/ad7d8b)
- Titarchuk, L. 1994, *ApJ*, 434, 570, doi: [10.1086/174760](https://doi.org/10.1086/174760)
- Titarchuk, L., & Fiorito, R. 2004, *The Astrophysical Journal*, 612, 988
- Titarchuk, L., & Osherovich, V. 1999, *ApJL*, 518, L95, doi: [10.1086/312083](https://doi.org/10.1086/312083)
- van der Klis, M. 2005, *Astronomische Nachrichten*, 326, 798, doi: [10.1002/asna.200510416](https://doi.org/10.1002/asna.200510416)
- Wijnands, R., Homan, J., & van der Klis, M. 1999, *The Astrophysical Journal*, 526, L33
- Wood, C. M., Miller-Jones, J. C. A., Bahramian, A., et al. 2023, *MNRAS*, 522, 70, doi: [10.1093/mnras/stad939](https://doi.org/10.1093/mnras/stad939)
- Xu, Y., & Harrison, F. 2021, *The Astronomer's Telegram*, 14609, 1

- Yadav, J. S., Agrawal, P. C., Antia, H. M., et al. 2016a, in Society of Photo-Optical Instrumentation Engineers (SPIE) Conference Series, Vol. 9905, Space Telescopes and Instrumentation 2016: Ultraviolet to Gamma Ray, ed. J.-W. A. den Herder, T. Takahashi, & M. Bautz, 99051D, doi: [10.1117/12.2231857](https://doi.org/10.1117/12.2231857)
- Yadav, J. S., Misra, R., Verdhhan Chauhan, J., et al. 2016b, ApJ, 833, 27, doi: [10.3847/0004-637X/833/1/27](https://doi.org/10.3847/0004-637X/833/1/27)
- Zdziarski, A. A., Szanecki, M., Poutanen, J., Gierliński, M., & Biernacki, P. 2020, MNRAS, 492, 5234, doi: [10.1093/mnras/staa159](https://doi.org/10.1093/mnras/staa159)
- Zhang, Z., Bambi, C., Liu, H., et al. 2024, ApJ, 975, 22, doi: [10.3847/1538-4357/ad7b29](https://doi.org/10.3847/1538-4357/ad7b29)
- Zhu, H., Chen, X., & Wang, W. 2023, MNRAS, 523, 4394, doi: [10.1093/mnras/stad1656](https://doi.org/10.1093/mnras/stad1656)